Japanese Journal of Applied Physics

The Japan Society of Applied Physics

REGULAR PAPER • OPEN ACCESS

InAlN-based LEDs emitting in the near-UV region

OPEN ACCESS

Japanese Journal of Applied Physics **58**, SCCB33 (2019) **REGULAR PAPER**

https://doi.org/10.7567/1347-4065/ab106b

InAlN-based LEDs emitting in the near-UV region

Pietro Pampili[1,2*], Vitaly Z. Zubialevich[1], Pleun Maaskant[1], Mahbub Akhter[1], Brian Corbett[1], and Peter J. Parbrook[1,2*]

[1]*Tyndall National Institute, University College Cork, Lee Maltings, Dyke Parade, Cork, Ireland*
[2]*Department of Electrical and Electronic Engineering, University College Cork, Cork, Ireland*

[*]E-mail: pietro.pampili@tyndall.ie; peter.parbrook@tyndall.ie

Received December 31, 2018; accepted February 27, 2019; published online May 23, 2019

Fully functional InAlN-based ultraviolet LEDs emitting at 340–350 nm were demonstrated for the first time; detailed electrical and optical characterization is presented and discussed. Results from the measurements at pulsed conditions are in agreement with the attribution of the dominant electroluminescence peak to near-band-edge emission. The composition of the AlGaN barriers was chosen to give the same internal polarization field as that of the InAlN wells. A simulation study of this polarization-matched heterostructure shows a significant increase in the electron-hole overlap integral if compared with a standard AlGaN/AlGaN active region having the same level of carrier confinement. Limitations and problems of these preliminary devices are also presented, and possible future work aimed at increasing their efficiency is discussed.

1. Introduction

Ultraviolet LEDs with emission wavelengths shorter than 365 nm almost exclusively use either AlGaN quantum wells[1)] (QWs), or InAlGaN ones with only small amounts of In.[2)] Compared with the InGaN QWs typical of visible or near-UV LEDs, AlGaN-based active regions suffer from a reduced degree of localization, which makes them quite sensitive to the dislocation density.

From this point of view, because of the localization effects due to the presence of In atoms, InAlN alloys with InN concentrations up to 40% have a great potential for their use as active materials in UV LEDs with emission spanning the whole ultraviolet range. However, due to the very different optimal growth conditions between its binary components InN and AlN, InAlN ternary alloys are still very difficult materials to grow, and, until now, they have found application almost exclusively in Bragg reflectors[3)] or high electron mobility transistors[4)] at compositions close to lattice-matching to GaN.

In the last few years, with the aim of extending the use of InAlN alloys also to light emitting applications, our group has extensively investigated the growth of InAlN materials in the range 0%–25% of InN content.[5–8)] PL experiments performed on our samples show broad peaks with full width at half maxima (FWHM) in excess of 200 meV, and "apparent" internal quantum efficiencies (i.e. low-temperature to room-temperature intensity ratios) up to 40%. These results are in agreement with the higher degree of localization that is expected from these alloys, and confirm their potential as light emitting materials.

Another significant advantage of using InAlN QWs in UV LEDs, is that the simultaneous use of AlGaN barriers adds a further degree of freedom in the design of the LED active region, whereby a "polarization-matched" heterostructure with reduced or null quantum confined stark effect can be achieved without losing confinement in the wells. A similar approach based on the use of quaternary InAlGaN alloys has already been proposed for visible devices;[9–11)] however, as polarization discontinuities are very detrimental also in AlGaN/AlGaN active regions,[12)] and even more so when Al-rich barriers are used to increase carrier confinement, this solution appears to be particularly suitable for UV LEDs.

In this paper we report, to the best of our knowledge for the first time, the demonstration of a fully operational InAlN-based UV LED, with AlGaN barriers designed to be close to polarization-matching to the InAlN QWs.

2. Experimental methods

2.1. Material growth

All the samples in this study were grown by metal organic vapour phase epitaxy (MOVPE) in an AIXTRON 3×2FT vertical reactor on top of low-defect-density AlN templates, which were previously deposited on 2 inch sapphire substrates following our standard approach, whose details have been reported elsewhere.[13)] Trimethylgallium, trimethylindium, trimethylaluminium and ammonia where used as precursors, while doping of the *n*- and *p*-type cladding layers was obtained using disilane (Si_2H_6) and bis-cyclopentadienyl magnesium (Cp_2Mg), respectively.

The active region, grown on top of a 1.5 μm thick *n*-$Al_{0.77}Ga_{0.23}N$ cladding layer, consisted of five $In_{0.14}Al_{0.86}N$ QWs sandwiched between $Al_{0.69}Ga_{0.31}N$ barriers with thickness of 1.85 and 6.0 nm, respectively. Because the growth temperature of the InAlN wells is significantly lower than the one commonly used for the AlGaN barriers (in our recipe 770 °C and 1010 °C, respectively) a low-temperature AlGaN capping layer of about 1 nm was grown immediately after each QW before increasing the temperature to barrier condition. The inclusion of this capping layer, which is kept as thin as possible to minimise any effects on the carrier transport, is necessary to avoid In desorption during the high-temperature growth of the barriers. Further details about this 2-temperature approach as well as all the details of the growth of the InAlN/AlGaN multiple quantum well structure can be found in our previously published paper on this topic.[5)] On top of the active region a *p*-$Al_{0.80}Ga_{0.20}N$ electron blocking layer, plus *p*-$Al_{0.70}Ga_{0.30}N$ and *p*-$Al_{0.55}Ga_{0.45}N$ cladding layers (12, 30, and 20 nm thick, respectively) were subsequently grown. Finally, on top of this

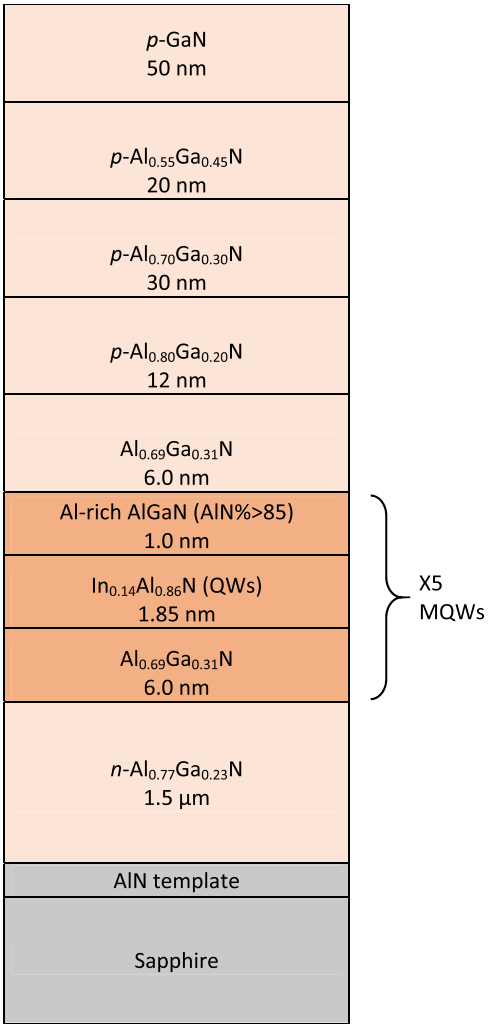

Fig. 1. (Color online) Schematics of the InAlN-based UV LED heterostructure grown by MOVPE.

structure a cap of 50 nm of *p*-GaN was deposited to allow good electrical contact. A schematic of the whole structure is shown in Fig. 1.

2.2. Device fabrication

After growth, the 2 inch wafers were diced into quarters, and devices were subsequently fabricated in the form of clusters of micron-sized emitters (μ-LED), following an approach that was developed at our institution, originally for visible devices,[14,15] but later successfully applied also to UV LEDs.[16,17] With this special implementation of the μ-LED concept, the individual emitters that compose the final device have smooth, reflective, and quasi-parabolically shaped sidewalls that are obtained by a specially optimized dry etch process, a configuration that allows the light emitted at larger angles to be reflected back, at almost perpendicular angles, towards the sapphire substrate. In this way, in addition to the better current injection and thermal management typical of μ-LEDs, our devices also have a significantly increased light extraction efficiency.

For the devices described in this paper, the process starts with a cleaning of the samples in room-temperature buffered oxide etch and HCl for five minutes each, followed by a 30 s dip in a solution of KOH in deionized water (45 wt%) at 90 °C, to remove oxides, metals and organic contaminants from the samples. After the cleaning, to avoid any re-oxidation, the samples are immediately prepared for the definition of the *p*-type contacts by photolithography. A Pd film of 40 nm is then deposited by e-beam evaporation and, after the lift-off of excess metal, the contacts left on the sample consist of clusters of dots having a diameter of 8 μm each that will become the tops of the μ-LED emitters. The following step is the dry etch necessary to expose the *n*-type cladding layer, followed by the subsequent deposition, also by e-beam evaporation, of a sequence of Ti/Al/Ti/Au contact metals, with thicknesses of 20, 170, 5 and 100 nm, respectively. No annealing treatment is included for either contact.

The next step is the definition of the μ-LED sidewalls by dry etch. Initially a thick resist is spin-coated on the sample, and then exposed to form sets of "cylinders" in correspondence of the *p*-contact dots. After development, the resist "cylinders," which have their diameter equal to the basal diameter of the final μ-LED, are reflown in oven at 140 °C for 3 to 4 h in order to obtain the parabolic sidewalls. The shape so obtained is then transferred into the material by means of a carefully optimized dry etch step with an etch selectivity between the resist and the AlGaN material of roughly 1:1. As the sidewall-shaping etch also exposes the edges of the active region, to avoid any risk of contamination, a passivation step is performed as soon as possible after having removed all the resist residues from the sample: typically 300 nm of SiO_2 is hence blanket-deposited by sputtering. Although the dry etch step may introduce non-radiative recombination centres on the emitter sidewalls, according to our previous experience with visible μ-LEDs,[14] this effect is not significant and no chemical treatment was hence included in the fabrication process at this stage. Openings in the passivation layer are then created, also by dry etch, in correspondence to the contacts. A final photolithographic step and subsequent evaporation of Ti/Au (30 and 300 nm, respectively) is necessary to electrically connect the *p*-contacts of all the μ-LEDs present in each cluster, and to define the metal pads necessary for wire-bonding or *on-chip* testing of the devices. A schematic of this fabrication process, as well as an SEM image of a cluster of μ-LEDs is shown in Fig. 2.

2.3. Characterization

For the electroluminescence (EL) characterization, the devices were contacted directly *on-chip* with a micromanipulator, and biased at different DC currents by means of a Keithley SourceMeter 2400 generator, while the corresponding voltage drops were recorded. During the measurement, the chip was held by a copper support that also served as a heatsink while the light was collected from its back side by means of a UV-transparent optical fibre through a small aperture in the support. The fibre was a step index, multimode one with a core diameter of 910 μm, and was held perpendicular to the chip and put in contact with the sapphire substrate just below the device under test, whose dimensions are $520 \times 520\ \mu m^2$. The light was then directed into a miniature Ocean Optics 2000 + UV–VIS spectrometer, and the relative spectral intensity of the different samples was recorded as a function of the current.

In order to gain a better understanding of the origin of the different peaks present in the EL spectra, a modulation bandwidth analysis was also carried out using a setup whose details have already been described elsewhere.[16] With this approach, the devices are again contacted *on-chip* by means of a micromanipulator, this time equipped with a coaxial

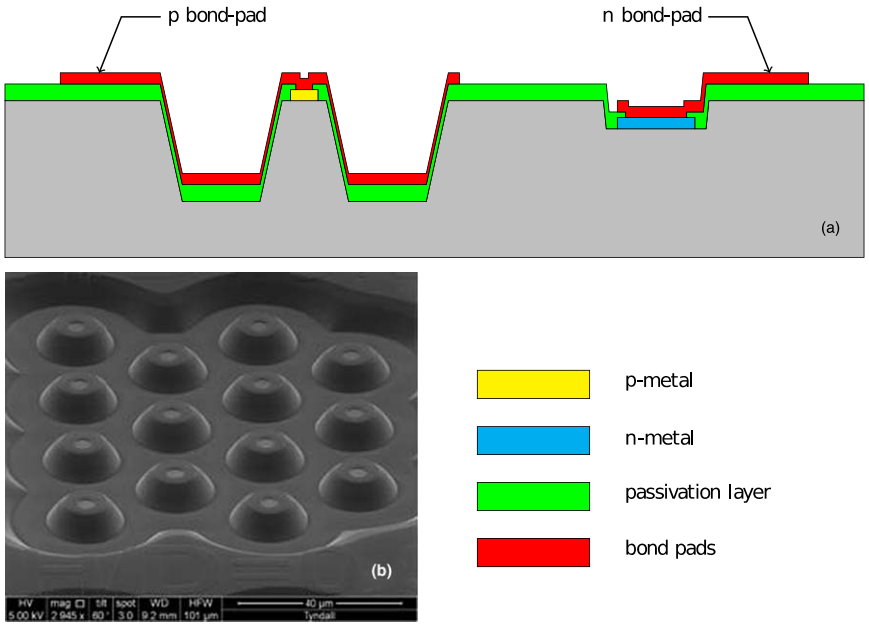

Fig. 2. (Color online) Schematics of the μ-LED fabrication sequence (a). For clarity, a Scanning Electron Microscopy image is also included (b), which shows a cluster of μ-LED emitters taken after the creation of the p-contact openings in the SiO_2 layer, but before the deposition of the bond-pad metal.

probe tip, and intermittently biased using a high-power pulse generator. The applied waveform consisted in a square function with a 0 V off-state and a 10 mA on-state. To avoid any heating up of the chip, the duty cycle was set to 1%, which corresponds to a repetition period of 100 μs. The light emitted by the device, and collected from below the wafer with the UV-transparent optical fibre, was brought to the entrance port of a Horiba iHR320 spectrometer equipped with a Hamamatsu R943-02 photomultiplier tube (PMT) for the time response measurements. To separately explore the switching characteristics of the two main EL peaks, the orientation of the diffraction grating was set to direct the light coming from the peak under investigation at the centre of the narrow exit-slits, so that all the other components of the spectral radiation could be stopped before entering the PMT. The small current from the PMT was then converted into a voltage signal with a 50 Ω resistance; the signal was averaged and conditioned to limit the effects of electromagnetic interferences, and the turn-on and turn-off transients recorded and analysed.

2.4. Simulations

In order to guide the design of the device, a series of simulations were also carried out using SiLENSe,[18] a commercial software package produced by STR. Although this programme comes with a material database that already contains all the relevant parameters for the III-nitride compounds and alloys, those proposed for InAlN need to be reviewed with great care, if reliable simulations of the devices based on this material are sought. In fact, because InAlN is still a relatively new material, its parameters reported in in literature are quite scattered, particularly the data about bandgap values as a function of the composition. As for the other III-nitride alloys, it is well-known that the bandgap (E_G) of InAlN does not follow a simple linear Vegard's law and that some form of correction is needed, usually implemented in terms of a bowing parameter b:

$$E_G(In_xAl_{1-x}N) = E_G^{In}x + E_G^{Al}(1-x) - bx(1-x). \quad (1)$$

However, there is no agreement about what bowing parameter should be used, with values ranging from 2.5 to 10 eV (for more details, see Ref. 19 and references therein). It is important to note that this parameter is a very critical one, because from it depends the possibility of realizing a polarization-matched InAlN/AlGaN structure having sufficient carrier confinement, or even which alloy would act as a barrier and which one as a well. In the most recent work, both theoretical and experimental, done at our research institute on this subject[6,19] it was proposed that the InAlN bandgap does not have a parabolic dependence on the composition and therefore, if expressed in the form of Eq. 1, the bowing parameter has to be strongly composition-dependent, which explains the large differences reported in literature. In this work we then used these new data, and, in order to obtain reasonable band offsets, we also set the electron affinity (E_{ea}) of InAlN to be:

$$E_{ea}(In_xAl_{1-x}N) = E_{ea}^{In}x + E_{ea}^{Al}(1-x) - b_{ea}x(1-x), \quad (2)$$

in which the electron affinity bowing parameter (b_{ea}) is defined as the 70% of the bandgap bowing parameter (b). This choice causes the composition-dependent correction of the Vegard's law to split into 70% to the conduction band and 30% to the valence band, an approximation that is in close agreement with the results of Ref. 19, and also frequently assumed in the simulations of III-nitride-based devices reported in literature.[20–22] On the contrary, it was not necessary to change the electron affinities of the binary compounds AlN, InN and GaN, which were left to the standard values of 0 eV, 3.85 eV and 1.96 eV, respectively, as these already satisfy the empirical rule of 70%–30% band-offset splitting. It is finally worth noting that these "electron affinity" values are used in SiLENSe with the only purpose of defining the band offsets, and might differ from the actual electron affinities as estimated from the work functions of the

Table I. Material parameters.

	AlN	GaN	InN
Lattice parameter c (nm)	0.4982	0.5186	0.5705
Lattice parameter a (nm)	0.3112	0.3188	0.3540
Stiffness constant C_{11} (GPa)	395	375	225
Stiffness constant C_{12} (GPa)	140	140	110
Stiffness constant C_{13} (GPa)	115	105	95
Stiffness constant C_{33} (GPa)	385	395	200
Stiffness constant C_{44} (GPa)	120	100	45
Spontaneous polarization P_z^s (C m^{-2})	−0.081	−0.029	−0.032
Piezoelectric tensor e_{33} (C m^{-2})	1.55	0.65	0.43
Piezoelectric tensor e_{31} (C m^{-2})	−0.58	−0.33	−0.22
Piezoelectric tensor e_{15} (C m^{-2})	−0.48	−0.33	−0.22
Dielectric constant ε_{33}	8.5	8.9	15.3
Bandgap E_G at $T = 0$ (eV)	6.25	3.51	0.69
Varshni parameter a (meV K^{-1})	1.799	0.909	0.404
Varshni parameter b (K)	1462	830	454
Crystal field splitting (eV)	−93.2	22.3	37.3
Spin-orbital splitting (eV)	11.1	11.1	11.1
AlGaN bowing parameter (eV)	1.0		—
Effective mass $m_n/m_0\perp$	0.25	0.2	0.1
Effective mass $m_n/m_0\parallel$	0.25	0.2	0.1
Effective mass $m_{lh}/m_0\perp$	1.95	1.1	1.35
Effective mass $m_{lh}/m_0\parallel$	0.25	0.15	0.1
Effective mass $m_{hh}/m_0\perp$	1.95	1.1	1.35
Effective mass $m_{hh}/m_0\parallel$	2.58	1.65	1.45
Effective mass $m_{so}/m_0\perp$	0.23	0.15	0.09
Effective mass $m_{so}/m_0\parallel$	1.93	1.1	1.54
Ionization energy (eV)	470	13	13

materials. All the other material parameters relevant to the simulations were kept to the standard values defined in the built-in database of the software SiLENSe, and are reported in Table I for clarity. These "standard" values are based on relevant literature reviews concerning lattice parameter,[23–25] elastic constant,[23,24,26,27] polarization constant,[24,28,29] energy gap,[30–32] bowing parameter,[33–36] valence band splitting,[37,38] effective mass,[37,38] and impurity ionization energy.[23,24,39]

Although the devices fabricated and characterized in this study are multi-QWs structures, the feasibility of the polarization-matched active region can be studied in single-QW devices all the same, which also have the advantage of greatly reducing the convergence problems that sometimes plague the simulations of more complicated devices. For this reason, the latter solution was adopted in all the simulations here described. A reference device, in which the InAlN QW was substituted with an AlGaN-based layer of the same bandgap, was also simulated for comparison; the details of both structures are summarized in Table II. A thin Al-rich layer inserted between the QW and the second barrier was included in the sequence to account for the capping layer that, as described in Sect. 2.1, is indispensable to avoid In desorption from the QWs during the growth of the actual devices.

Finally, to gain some indication about the magnitude of the increase in internal quantum efficiency that a perfectly polarization-matched active region would be able to provide, the overlap integrals of the electron and hole wavefunctions were calculated. This was also done with SiLENSe, by activating an optional module that uses as input data the shapes of the conduction and valence bands, which in turn come from the solutions of the standard drift-diffusion simulation at any current density, and numerically solves the Schrödinger equation for electrons and holes (in all the subbands).

3. Results and discussion

3.1. Polarization-matched structure

The band diagrams of the polarization-matched and reference AlGaN/AlGaN LEDs are shown in Figs. 3(a) and 3(b), respectively, when no bias is applied to the devices. The bending of the barriers in both structures is caused by the built-in potential only, as the polarization fields are screened by the free carriers. In the reference device, however, the thin QW has an internal polarization that greatly differs from that of the surrounding barriers, and the charges that form at the interfaces cannot be screened. The resulting electric field causes the well to strongly bend downwards. When some bias is applied to the devices, the band diagrams start to flatten and increasingly higher currents to flow through them; when a value of 100 A cm^{-2} is reached, both devices have almost completely flat conduction and valence bands. On the contrary, in the region between the n- and p-layers, the two devices behave quite differently: while in the polarization-matched LED the bending of the QW follows that of the barriers, in the reference structure the external bias only causes the QW band edges to bend even further, as shown in Figs. 3(c) and 3(d).

To better illustrate the reason of this behaviour, the spontaneous, piezoelectric, and total polarization fields present in the two structures are shown in Figs. 4(a) and 4(b). Assuming that both active regions are fully strained to the cladding layers, the piezoelectric polarization, caused by the elastic deformations necessary to preserve the in-plane lattice constant, is added to the already present spontaneous polarization. However, while in the polarization-matched device the variations of spontaneous and piezoelectric polarization have opposite signs and cancel each other, in the reference device they add up and the discontinuity in the total polarization becomes even stronger. The resulting electric fields are shown in Figs. 4(c) and 4(d), where the differences in the two QW systems are apparent.

Table II. Summary of the simulated structure.

Layer	Material and composition	Thickness (nm)	N_A or N_D (cm^{-3})
Contact enhancer	p-GaN	30	2×10^{18}
Cladding layer	p-$Al_{0.53}Ga_{0.47}N$	70	2×10^{18}
Quantum barrier	$Al_{0.53}Ga_{0.47}N$	6.5	—
Capping layer	$Al_{0.85}Ga_{0.15}N$	0.5	—
Quantum well	$In_{0.14}Al_{0.86}N$ or $Al_{0.39}Ga_{0.61}N$	2	—
Quantum barrier	$Al_{0.53}Ga_{0.47}N$	9	—
Cladding layer	n-$Al_{0.53}Ga_{0.47}N$	500	2×10^{18}

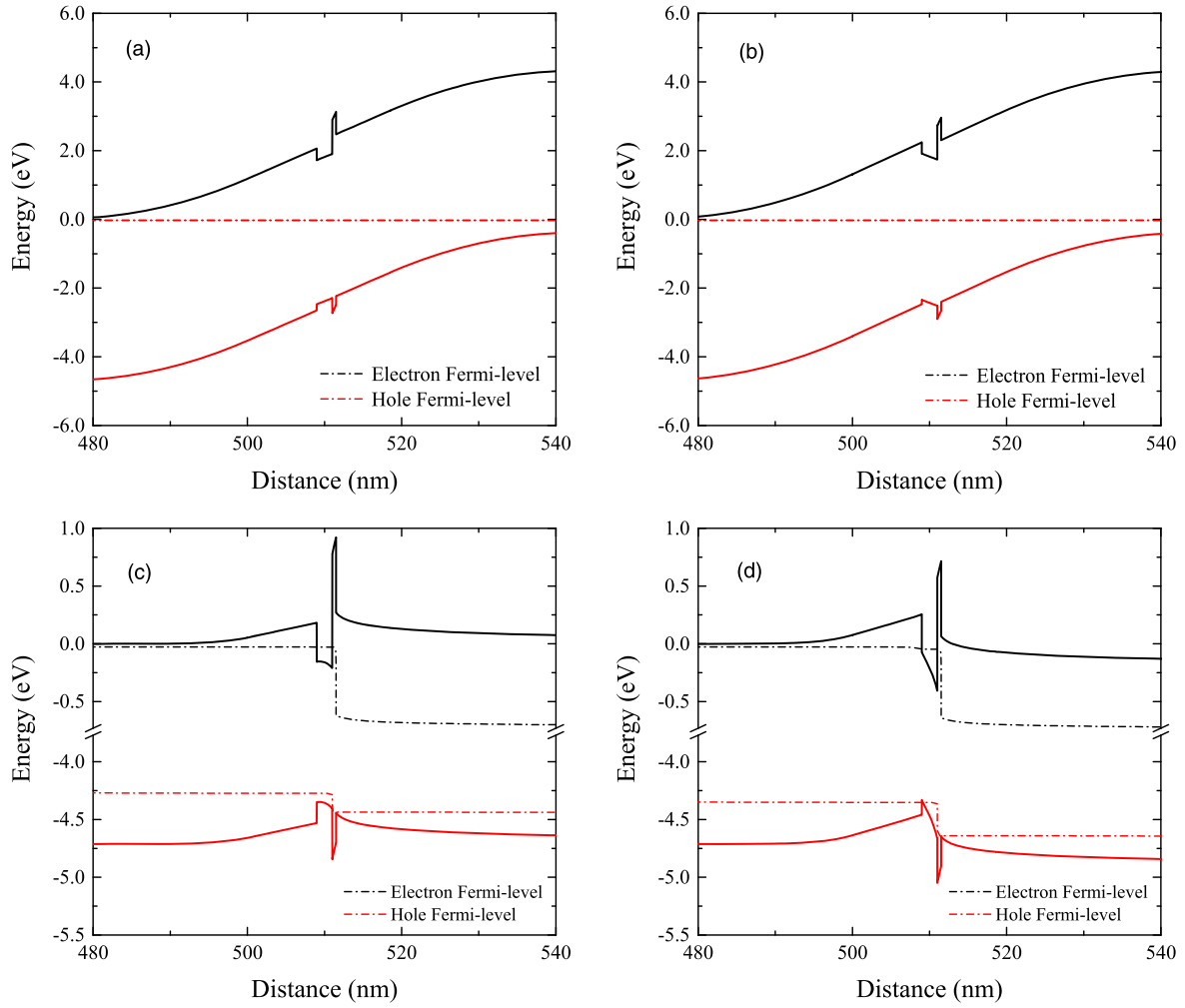

Fig. 3. (Color online) Band diagram of the InAlN/AlGaN UV LED emitting at 340 nm (a), and that of a standard AlGaN/AlGaN device emitting at the same wavelength (b), when no bias is applied. Close-up of the conduction and valence bands at 100 A cm^{-2} of the InAlN (c), and the AlGaN-based (d) LEDs.

Using the band diagrams obtained with a current density of 100 A cm^{-2}, the wavefunctions of electrons and heavy, light, and split-off holes were calculated as shown in Fig. 5. Although the presence of the wide-bandgap capping layer is able to partially limit the deformation of the electron wavefunction, the shift in the peak positions of all the hole wavefunctions is clearly visible. The values of the overlap integrals computated by SiLENSe are reported in Table III, and show an increase of the recombination rates from 55% up to 91% with respect to the reference device.

Hence, this initial simulation work demonstrated the feasibility of a polarization-matched near-UV InAlN/AlGaN structure emitting at 340 nm by proving that this approach is compatible with the most recent theoretical studies about InAlN, and guided the subsequent experimental work.

3.2. Device characterization under DC conditions

During the study, various growth and fabrication runs were carried out, which gave quite different results as can be seen in Fig. 6, where the IV characteristics of three typical samples are compared. In the initial runs, the best samples had behaviours similar to the one shown for sample #1. Despite having a somewhat high turn-on voltage, these samples were able to produce some EL emission at the expected wavelength, although of rather low intensity if compared with the emission of standard AlGaN/AlGaN deep-UV LEDs realized with the same fabrication process. Device stability was an issue for some devices as illustrated for example by sample #2, where no EL emission was observed for the low voltage situation. In a few samples (not shown here) the instability presented a series of jumps back and forth between the initial and the final IV characteristics, with concurrent series of drops and recoveries of the EL emission. This behaviour suggests that the degradation of the devices did not involve the destruction of the active region, but it was most likely due to the presence of some short-circuit path caused by contact or cladding layer issues that caused a reduction in the injection of the carriers into the QWs.

A second full growth and fabrication run, after some optimization work that included a full revision of the *p*-type-doped cladding structure, gave the final version of the device as described in Sects. 2.1 and 2.2. The IV characteristics of the LEDs fabricated during this final run are exemplified by sample #3 of Fig. 6. Despite having a more than doubled voltage drop, these devices proved to be much more stable, with no changes in the IV characteristics even after repeated tests. In addition to that, they also showed the EL emission with the highest intensity among all the runs of this project.

An example of the typical EL spectra from the samples of this final run is shown in Fig. 7 for different currents in the range 1–14 mA, corresponding to a current density range of 100–1400 A cm^{-2}. In addition to the targeted near-UV peak at 340–350 nm due to near-band-edge (NBE) emission from

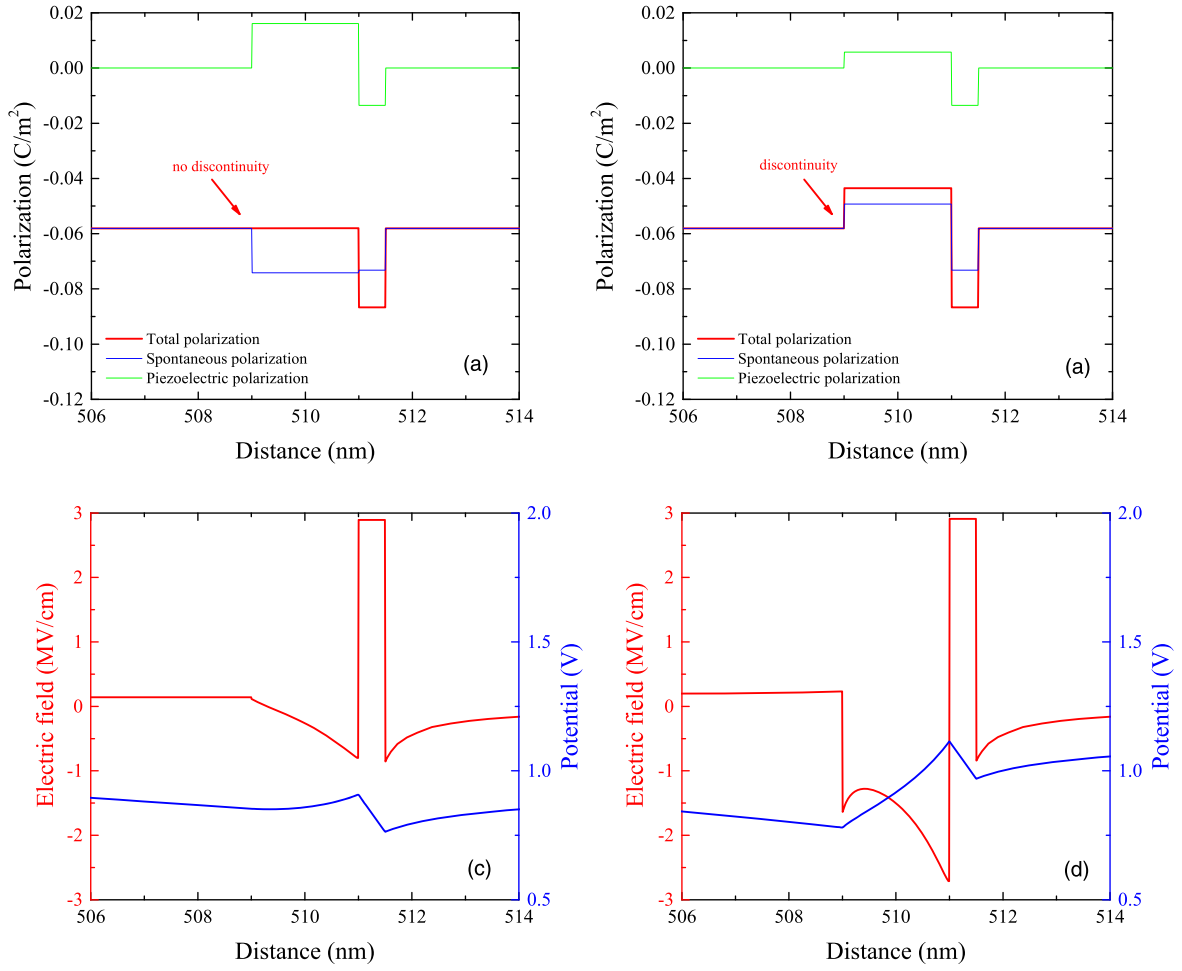

Fig. 4. (Color online) Spontaneous, piezoelectric and total polarization fields of the InAlN/AlGaN UV LED emitting at 340 nm (a), and that of a standard AlGaN/AlGaN device emitting at the same wavelength (b). Electric field and potential of the InAlN (c), and the AlGaN-based (d) LEDs.

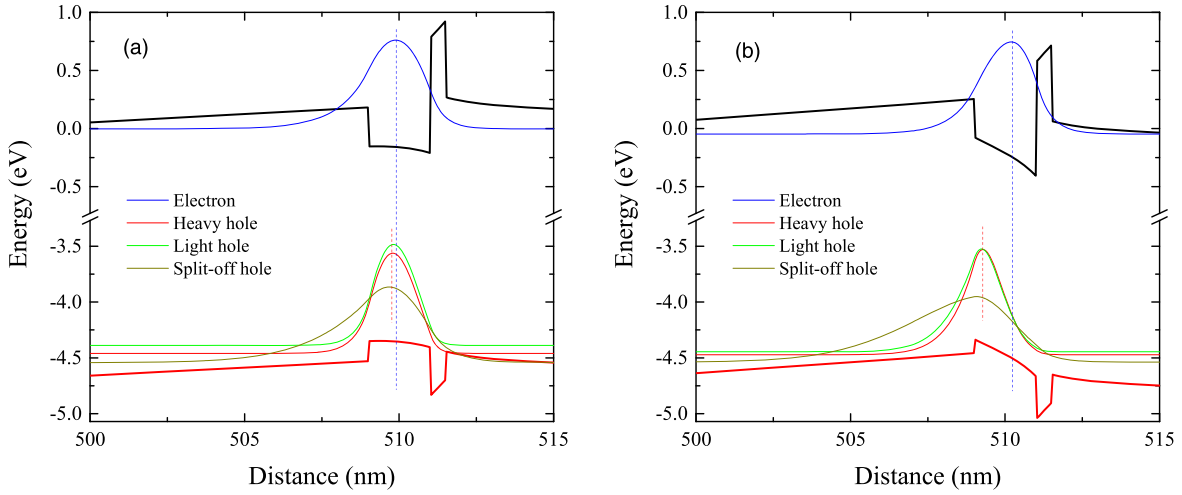

Fig. 5. (Color online) Carrier wavefunctions calculated by SiLENSe for the band position at 100 A cm^{-2} in the InAlN/AlGaN UV LED emitting at 340 nm (a), and in the standard AlGaN/AlGaN device emitting at the same wavelength (b).

Table III. Overlap integrals.

	Electrons/Heavy holes	Electrons/Light holes	Electrons/Split-off holes
InAlN/AlGaN LED	0.9398	0.9300	0.9347
AlGaN/AlGaN LED	0.6045	0.5681	0.4885

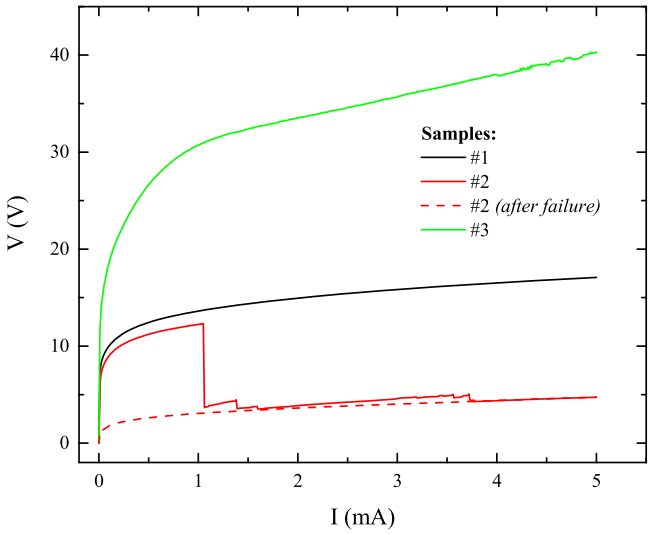

Fig. 6. (Color online) IV characteristics of three typical InAlN-based UV LEDs produced and tested at different stages of the project. Data relative to sample #2 are reported both before and after its irreversible failure.

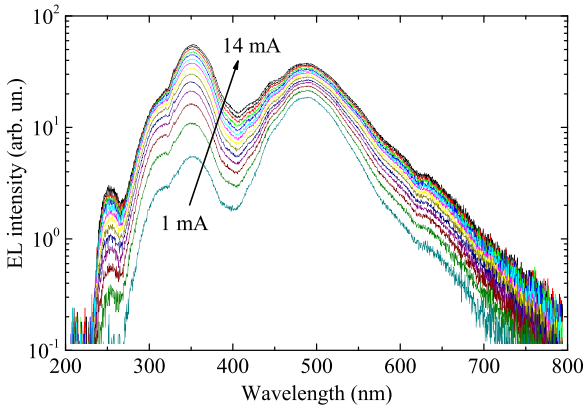

Fig. 7. (Color online) Typical EL spectra of the InAlN-based UV LED collected at different current biases in the range 1–14 mA.

the QWs, a large peak at about 490 nm and a second weak peak at about 250 nm were also present. Based on a preliminary photoluminescence (PL) and photoluminescence excitation (PLE) study[5] of InAlN/AlGaN quantum well structures similar to those used in the final device, we believe the emission at about 490 nm is most likely due to deep level emission in the AlGaN barriers. In fact, while PL data clearly show a peak in this position, its intensity was significantly lower when the excitation energy was decreased below the absorption edge of the AlGaN barriers.

While the NBE peak initially showed significantly lower intensity than the main defect-related peak, at currents higher than 4 mA it eventually became the dominant one. As the current was increased the voltage also kept increasing almost linearly, reaching the very high value of over 50 V at 14 mA. Only at higher currents did the devices start to become somewhat unstable, and ultimately at even higher currents, they eventually failed irreversibly. Although not conclusive, post-failure analysis seems to suggest the failure is related to the loss of insulation from the SiO_2 passivation layer in small areas close to the edge of the μ-LEDs, which might be due to the high working voltages of these devices, a serious problem that needs to be addressed in future work.

It is worth noting that the NBE emission at 340–350 nm is very significantly red-shifted from the emission one would simplistically expect from a material having a bandgap of 4.2 eV, as is the case with the $In_{0.14}Al_{0.86}N$ QWs of our device.[6,19] However, based on our previous PL studies on this topic[5] this behaviour is as expected for InAlN alloys of this composition. In those studies the PL peaks from InAlN QWs having InN concentrations in the range 12%–18% were observed to be red-shifted by up to 0.52 eV below the absorption edge measured by PLE spectroscopy. This large Stokes shift is a clear signature of the expected high degree of localization in this material (due to the much larger bandgap difference in the binary endpoints of 5.5 eV compared to AlGaN or InGaN, which is in addition to any non-random alloy effects due to local lattice strain that may occur). This high localisation confirms the reason for choosing InAlN alloys as active materials for light emission. In further support of this argument, one can also observe that the FWHM of the NBE emission is much larger than the typical FWHM of AlGaN/AlGaN QWs, again, in agreement with our previous PL studies,[7] in which FWHM in the 0.3–0.5 eV range were reported due to the localisation effects in this alloy.

Finally, another interesting aspect of the spectra shown in Fig. 7 is the presence of a small peak at 250 nm, and a shoulder emission at around 310 nm, which were not evident in any of the preliminary PL study. This fact indicates the presence of carrier recombination in some areas other than the wells, most likely either the barriers or the electron blocking layer, suggesting that further work to optimise carrier transport in the active region is required.

3.3. Modulation bandwidth (pulsed conditions)

Modulation bandwidth measurements as described in Sect. 2.3 were then attempted for all the three EL peaks. While the emission at about 250 nm was too weak to be analysed, the other two peaks (i.e. the NBE emission at about 340 nm, and the defect-related emission at about 490 nm) were of sufficient intensity to be acquired and averaged over reasonable lengths of time. An example of the typical transients obtained for these LEDs is shown in Fig. 8, in which the data relative to both emission peaks were collected from the same device and with the same optical-fibre coupling. As can be seen in Fig. 8(a), the emission at 340 nm also shows an initial intensity maximum whose value is more than two times of the asymptotic level reached about 200 ns after the turn-on. The origin of this intensity drop is still not fully understood; however, a somewhat similar behaviour has been previously observed in AlGaN-based UV LEDs and attributed to the onset of a competing recombination channel in the *p*-AlGaN cladding layer after a retarded ionization of the acceptor states.[40] The presence of a similar recombination mechanism in our devices would be responsible for a reduced hole injection in the QWs, and need to be further investigated.

Despite the noise present in these data, it was still possible to estimate the optical modulation bandwidth of the main peak by using the method described in Ref. 16, and values as high as 42 MHz were measured, a result that is consistent with our attribution of this peak to NBE emission. Although the presence of large ringing oscillations caused by the impedance mismatch between power generator and device

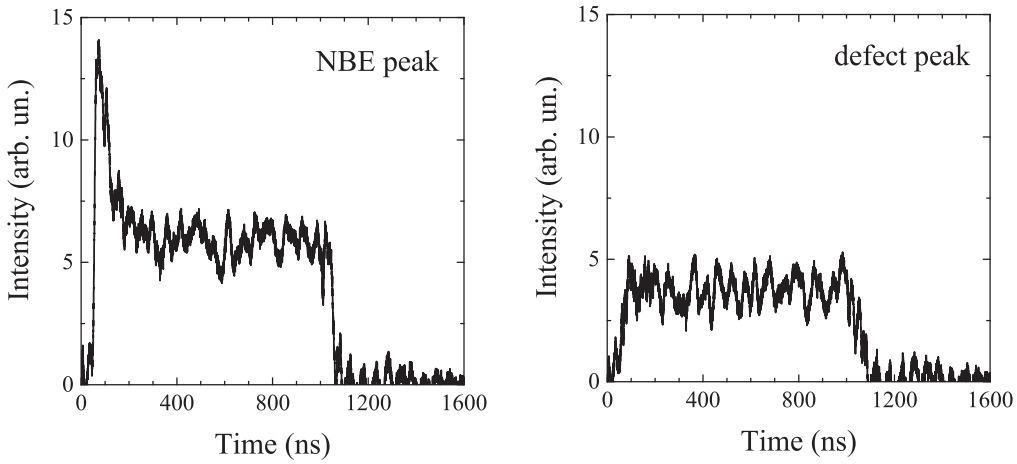

Fig. 8. Transients from the modulation of the InAlN-based UV LED relative to the 340 nm peak (a) and the 490 nm peak (b), reconstructed through the averaging of the signal coming from the PMT and the subtraction of electromagnetic interferences.

made it impossible to extend the same quantitative analysis also to the peak at 490 nm, as can be seen in Fig. 8(b), both turn-on and turn-off times appear to be significantly larger than those of the main peak, as expected from a defect-related recombination mechanism.

4. Conclusions

In this work we have reported the first demonstration of a UV LED with an InAlN/AlGaN active region designed to be close to polarization-matching. The device, which for improved light extraction efficiency was fabricated using a μ-LED approach, showed a strong EL emission around 340–350 nm. Modulation bandwidth measurements performed both on the main emission peak and on the longer-wavelength one are in agreement with our assignation of the former to NBE recombination. The overall efficiency of this preliminary device is not yet comparable to our AlGaN/AlGaN standard LEDs emitting in the same range. However, the presence of a large voltage forward-drop as well as some emission at 250 nm, indicate that there is still scope for a great deal of improvement in the IV characteristics (contacts and cladding layers) and in the design of an optimized electron blocking layer for a more efficient reduction of leakage. Despite these problem, the final LED proved to be quite robust and with a stable emission, even at the highest voltage biases used for this characterization (up to more than 50 V).

Acknowledgments

This research was enabled by the Irish Higher Education Authority Programme for Research in Third Level Institutions Cycles 4 and 5 via the INSPIRE and TYFFANI projects, and by Science Foundation Ireland (SFI) under Grant No. SFI/10/IN.1/I2993. Peter J. Parbrook acknowledges funding from SFI Engineering Professorship scheme (SFI/07/EN/E001A).

ORCID iDs

Pietro Pampili https://orcid.org/0000-0003-4163-4475
Vitaly Z. Zubialevich https://orcid.org/0000-0003-4783-5104
Brian Corbett https://orcid.org/0000-0002-9002-8212
Peter J. Parbrook https://orcid.org/0000-0003-3287-512X

1) M. Kneissl, in *III-Nitride Ultraviolet Emitters*, ed. M. Kneissl and J. Rass, (Springer, Cham, 2016) Vol. 227, p. 1.
2) H. Hirayama, Y. Enomoto, A. Kinoshita, A. Hirata, and Y. Aoyagi, Appl. Phys. Lett. **80**, 1589 (2002).
3) J. F. Carlin and M. Ilegems, Appl. Phys. Lett. **83**, 668 (2003).
4) A. Dadgar, F. Schulze, J. Biäsing, A. Diez, A. Krost, M. Neuburger, E. Kohn, I. Daumiller, and M. Kunze, Appl. Phys. Lett. **85**, 5400 (2004).
5) V. Z. Zubialevich, T. C. Sadler, D. V. Dinh, S. N. Alam, H. Li, P. Pampili, and P. J. Parbrook, J. Lumin. **155**, 108 (2014).
6) V. Z. Zubialevich, D. V. Dinh, S. N. Alam, S. Schulz, E. P. O'Reilly, and P. J. Parbrook, Semicond. Sci. Technol. **31**, 025006 (2015).
7) V. Z. Zubialevich, S. N. Alam, H. N. Li, and P. J. Parbrook, J. Phys. D **49**, 385105 (2016).
8) V. Z. Zubialevich, M. V. Rzheutski, H. Li, T. C. Sadler, S. N. Alam, V. Bhardwaj, E. V. Lutsenko, G. P. Yablonskii, and P. J. Parbrook, J. Lumin. **194**, 797 (2018).
9) W. C. Lai, S. J. Chang, M. Yokoyam, J. K. Sheu, and J. F. Chen, IEEE Photonics Technol. Lett. **13**, 559 (2001).
10) M. F. Schubert, J. Xu, J. K. Kim, E. F. Schubert, M. H. Kim, S. Yoon, S. M. Lee, C. Sone, T. Sakong, and Y. Park, Appl. Phys. Lett. **93**, 041102 (2008).
11) Y. K. Kuo, M. C. Tsai, and S. H. Yen, Opt. Commun. **282**, 4252 (2009).
12) T. M. Al Tahtamouni, A. Sedhain, J. Y. Lin, and H. X. Jiang, Appl. Phys. Lett. **90**, 221105 (2007).
13) H. Li, T. C. Sadler, and P. J. Parbrook, J. Cryst. Growth **383**, 72 (2013).
14) P. Maaskant, E. A. O'Carroll, P. M. Lamkin, and B. Corbett, European Patent EP 1620902 B1 (2010).
15) P. P. Maaskant, H. Shams, M. Akhter, W. Henry, M. J. Kappers, D. Zhu, C. J. Humphreys, and B. Corbett, Appl. Phys. Express **6**, 022102 (2013).
16) M. Akhter, P. Pampili, V. Z. Zubialevich, C. Eason, Z. H. Quan, P. P. Maaskant, P. J. Parbrook, and B. Corbett, Electron. Lett. **51**, 354 (2015).
17) P. Pampili, M. Akhter, C. Eason, V. Z. Zubialevich, P. P. Maaskant, Z. Quan, P. O'Brien, B. Corbett, and P. J. Parbrook, IEEE Summer Topicals Meeting Series (SUM 2015), 2015, p. 177.
18) SiLENSe 5.4 Laser Edition, STR Group Inc. [str-soft.com].
19) S. Schulz, M. A. Caro, L. T. Tan, P. J. Parbrook, R. W. Martin, and E. P. O'Reilly, Appl. Phys. Express **6**, 121001 (2013).
20) T. H. Yu and K. F. Brennan, J. Appl. Phys. **89**, 3827 (2001).
21) O. Ambacher et al., J. Appl. Phys. **87**, 334 (2000).
22) G. Martin, S. Strite, A. Botchkarev, A. Agarwal, A. Rockett, H. Morkoç, W. R. L. Lambrecht, and B. Segall, Appl. Phys. Lett. **65**, 610 (1994).
23) I. Akasaki and H. Amano, Jpn. J. Appl. Phys. 1 **36**, 5393 (1997).
24) O. Ambacher, J. Phys. D **31**, 2653 (1998).
25) M. Leszczynski, T. Suski, H. Teisseyre, P. Perlin, I. Grzegory, J. Jun, S. Porowski, and T. D. Moustakas, J. Appl. Phys. **76**, 4909 (1994).
26) M. Van Schilfgaarde, A. Sher, and A. B. Chen, J. Cryst. Growth **178**, 8 (1997).
27) K. Shimada, T. Sota, and K. Suzuki, J. Appl. Phys. **84**, 4951 (1998).
28) V. W. L. Chin, T. L. Tansley, and T. Osotchan, J. Appl. Phys. **75**, 7365 (1994).
29) S. N. Mohammad and H. Morkoç, Prog. Quantum Electron. **20**, 361 (1996).
30) I. Vurgaftman and J. R. Meyer, J. Appl. Phys. **94**, 3675 (2003).
31) J. Wu and W. Walukiewicz, Superlattices Microstruct. **34**, 63 (2003).
32) V. Yu Davydov et al., Phys. Status Solidi B **229**, R1 (2002).

33) S. Stepanov, W. N. Wang, B. S. Yavich, V. Bougrov, Y. T. Rebane, and Y. G. Shreter, MRS Internet J. Nitride Semicond. Res. **6**, e6 (2001).
34) H. Angerer et al., Appl. Phys. Lett. **71**, 1504 (1997).
35) O. Katz, B. Meyler, U. Tisch, and J. Salzman, Phys. Status Solidi A **188**, 789 (2001).
36) F. Yun, M. A. Reshchikov, L. He, T. King, H. Morkoç, S. W. Novak, and L. Wei, J. Appl. Phys. **92**, 4837 (2002).
37) S. Chuang and C. Chang, Physical Review B **54**, 2491 (1996).
38) D. Dugdale, S. Brand, and R. Abram, Physical Review B **61**, 12933 (2000).
39) V Bougrov, M. E. Levinshtein, S. L. Rumyantsev, and A. Zubrilov, in *Properties of Advanced Semiconductor Materials*, ed. M. E. Levinshtein, S. L. Rumyantsev, and M. S. Shur, (Wiley, New York, 2001), Chap. 1.
40) M. Shatalov et al., Appl. Phys. Lett. **82**, 167 (2003).